Thesis for the Master's degree in Microtechnology

High Frequency Properties of the Oxide materials at millikelvin temperatures for HTS devices in the quantum limit

Mudassar Mumtaz Vrik

Supervisors:
Dr. Thilo Bauch
Dr. Florian Lombardi

Department of Microtechnology and Nanoscience
Chalmers University of technology
Gothenburg, Sweden 2009

Dedicated to my parents and siblings

Contents

Chapter 1

Introduction

Quantum computation deals with the processing of information according to the laws of quantum mechanics. Within the last few years, it has attracted considerable attention because quantum computers are expected to be capable of performing certain computational tasks much faster as compare to any other classical computer.

The idea of quantum computer arose from a simple question, “Can we simulate any quantum mechanically system using classical computers?”, came into the minds of scientists a long time before. The answer of this question is “NO”. This is called hidden-variable theorem which can be described as “Quantum systems cannot be simulated by classical universal computers” [Bell 1964].

In 1982, Richard Feynman was among the first to attempt to provide an answer to this question by producing an abstract theoretical model. He described how a quantum system could be used to do computations. Furthermore, he explained how such a machine would be able to act as a simulator for quantum physics [1]. In 1985 David Deustch proposed a simple algorithm exploiting quantum information to solve a model problem inherently faster than could be done classically [2]. It was the first demonstration that the richer physics available to a quantum computer might allow it to perform faster than a classical computer. Later, in 1994 Peter Shor designed algorithms specifically for quantum computers which could factor and take discrete logarithms of huge numbers, much faster than the best known classical algorithms [3].

Like a classical bit a quantum bit or qubit is a unit of quantum information and a basic building block of quantum computers. A classical bit can be made from any system with two states e.g. a MOSFET transistor. Similarly, a quantum bit or qubit can be created from any two quantum states like “0” and “1” as shown in figure 1(a). The main difference between a classical bit and quantum bit is that unlike a classical bit a qubit can not only exist in “0” or “1” state but also in superposition of these two states. A qubit state can be illustrated as a unit vector on the Bloch Sphere as shown in figure 1. Any point on this sphere shows a qubit state.

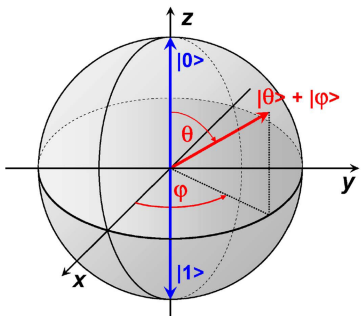

Figure 1 Illustration of the qubit state as a unit vector on the Bloch Sphere.

Multiple qubits have to be coupled to perform quantum computations. Microfabricated structures such as quantum dots and superconducting islands or loops are one way to implement these qubits. Superconducting microfabricated qubits, made with Josephson junctions (JJs), have the advantage compared to other systems because they could be easily coupled. This makes them appealing from the point of view of controllability, scalability and readout. In such kind of qubits information is stored in either charge on a nanoscale superconducting island, the flux or phase drop in a circulating current, or in the energy levels of a single junction. One of the main drawbacks of these kinds of devices is short coherent times caused by two sources of noise. One is the energy relaxation (at qubit transition frequency, 5-20GHz) within the dielectrics on which these devices are fabricated [4] and the other is dephasing (low frequency source of noise).

In 2005 M. H. S. Amin [5] proposed a Silent phase qubit based on YBCO JJs in the form of dc SQUID. He reported that the operating point of these qubits can be better protected from low frequency noise due to the doubly degenerate ground states in each of the junction of the SQUID. One can also think that the nodal quasi particles due to d-wave order parameter symmetry of YBCO can enhance the dissipation mechanism. Thilo Bauch studied the quantum dynamics of d-wave JJ and observed the energy level quantization [6] and macroscopic quantum tunneling [7] in these JJs which is a clear indication that the dissipation in a d-wave JJ is low enough to allow the formation of the sharp energy levels required for the qubit. These observations are encouraging for the engineering of novel quantum systems based on d-wave symmetry superconductors.

In recent years one main source of relaxation processes in qubits could be identified in the dielectric loss of any kind of insulators such as substrates and dielectric films used for capacitors and interconnecting layers. Therefore relaxation due to dielectric losses is still main hurdle in the way of LTS & HTS qubits which operate in the low temperatures (mK) and low powers (signle photon excitation) regime. Dielectric losses may be small at higher temperatures and higher powers and large at low temperatures and powers [8]. This kind of behavior can be understood by using two level states (TLS) defect model in dielectrics. These two level states in the dielectric are not saturated at low powers and low temperatures but become saturated at higher powers and temperatures by thermal bath or microwave powers. Saturated TLS do not contribute any longer to the dielectric losses. So, one needs to characterize these dielectrics at extremely low temperatures and low powers in order to detect all decoherence sources in the dielectric materials. In this

master thesis dielectric losses of MgO, which is suitable for epitaxial growth of YBCO, have been reported at low temperatures, low powers and high frequencies because loss mechanisms of MgO have up to now not been investigated at millikelvin temperatures and single photon excitations microwave powers before.

Grain boundary junctions fabricated by the biepitaxial technique is the most common way to make high quality JJs in HTS suitable for quantum circuit applications[9]. In biepitaxial technology single crystal substrates are used and a thin film of a suitable material, called seeding layer, is epitaxially grown partially on the top of its surface. The film deposited on such a structure has different crystal orientations depending on whether the deposition occurs on seed layer region or on bare substrate[10]. So a grained boundary JJ is formed at edge of seed layer. In case of YBCO strontium titanate (STO) is used as seed layer on a MgO substrate where the junction is formed at the interface between (001) YBCO films grown on (110) MgO substrate and (103) oriented films grown on STO layer. The dielectric properties of the substrate, together with the seed layer, are also important for the realization of such kind of single JJs based qubits. So the dielectric losses of MgO, with a thin layer of STO atop, are also discussed.

To enable measurements at high frequencies, films are often fabricated into strip line microstrip resonators. In this thesis we used coplanar wave guide resonator (CPW) technique for many different reasons.

- Coplanar waveguides have a simple layer structure without any deposition of insulator layer.
- It has better planar connection with quantum circuits.
- Resonance frequency of coplanar waveguide transmission lines is less sensitive to the kinetic inductance of the films as compared to the geometrical inductance of the structure.
- For a given substrate with certain thickness, different cross sections of transmission line with constant characteristic impedance $Z_L=50\Omega$ can be designed to match the resonator impedance with the impedance of all coaxial cables used in measurement setup and other microwave equipment.

A CPW resonator is constituted by a conductor separated from a pair of ground planes, all on the same plane, atop a dielectric medium and coupling capacitors to couple the resonators with the outside world. In this thesis quarter wavelength resonators, with interdigitated coupling capacitors at one end and shorted at the other, are made. Such types of resonators are characterized by measuring the reflection coefficient S_{11}. Once we have the S_{11} parameter the total quality factor Q_{tot} of the resonator can easily be calculated whose reciprocal is the sum of the reciprocals of the internal and external quality factors of the resonator. By extracting the external quality factor we can find the internal quality factor which is mainly due to the dielectric losses.

Information about the magnetic penetration depth λ_L of the films has been obtained from temperature dependent measurements of the resonance frequencies of the resonators.

Chapter 2

Transmission Lines and Waveguides

The purpose of uniform transmission lines is to transfer energy from a source to a destination. They can be of various types depending upon the application and the band of microwave or millimeter-wave frequency used. The length of a transmission line may vary from a fraction of a wavelength, in lumped element applications, to several wavelengths in distributed element circuitry. In general, transmission lines consist of two or more parallel conductors and support the propagation of transverse electromagnetic (TEM) waves. For a TEM wave the electric field $\boldsymbol{E}$ is perpendicular to both, the magnetic field $\boldsymbol{B}$ and the direction of propagation $\boldsymbol{k}$.
Now we will discuss the theory of transmission line in detail. The used equation and further information can be found in the reference [11] & [12].

2.1 Waves on a Lossy Transmission Line:

A transmission line is often schematically represented as a two-wire line, since transmission lines usually consist of two parallel conductors as shown in figure 2.1 (a). The conductors extend from $z = 0$ to infinity, thus forming a semiinfinite transmission line. At $z = 0$ a voltage generator with internal resistance R_g, is connected to the transmission line. The generator produces a voltage $V_g(t)$ that is impressed across the transmission line. If the generator is switched on at time $t = 0$, a current $I(t)$ will begin to flow into the upper conductor. A return current $-I(t)$ must then flow on the lower conductor since current flow through the generator must be continuous. The return current is produced by the action of the electric field established between the two conductors. Since the transmission line is semiinfinite in length, there is no direct conducting path between the upper and lower conductors. However, there is a distributed capacitance C per meter between the two conductors. As this electric field produces a magnetic field around the conductors so the there is a inductance L per unit length distributed across the transmission line. A short segment dz of the transmission line can be modeled as a lumped element circuit which includes a series inductance $L\,dz$ and a shunt capacitance $C\,dz$. As we are considering here a lossy transmission line so we have to add a series resistance R per unit length due to the finite conductivity of the

conductors. To be maintained parallel to each other, normally a dielectric material is used between the two conductors of the transmission line. These dielectric materials usually have a negligible conductance but do have a small amount of dielectric loss due to the polarization loss in the dielectric so we also have to add shunt conductance *G* per meter to account for this loss. The lumped element circuit model is show in figure 2.1 (b).

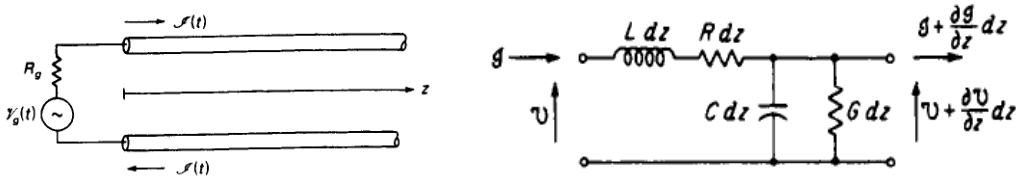

Figure 2.1 (a) A lossy two conductor transmission line connected to a voltage generator. (b) equivalent circuit of a differential section of the transmission line[11].

Voltage and current waves propagate with finite velocity on the transmission line when the generator is switched on. The equations that describe these waves are established by applying Kichhoff's circuit laws to the equivalent circuit of the differential section of transmission line which is shown in figure 2.1 (b). If the current and voltage at the input are *I (z,t)* and *V (z,t)* respectively and at the output are

$$V(z,t)+\frac{\partial V(z,t)}{\partial z}dz \qquad I(z,t)+\frac{\partial I(z,t)}{\partial z}dz.$$

Then according to Kirchoff's voltage law;

$$V(z,t)-\left(V(z,t)+\frac{\partial V(z,t)}{\partial z}dz\right)=I(z,t)Rdz+Ldz\frac{\partial I(z,t)}{\partial t},$$

or

$$\frac{\partial V(z,t)}{\partial z}=-I(z,t)R-L\frac{\partial I(z,t)}{\partial t}. \qquad (2.1)$$

Similarly, according to Kirchoff's current law;

$$I(z,t)-\left(I(z,t)+\frac{\partial I(z,t)}{\partial z}dz\right)=V(z,t)Gdz+Cdz\frac{\partial V(z,t)}{\partial t},$$

or

$$\frac{\partial I(z,t)}{\partial z}=-V(z,t)G-C\frac{\partial V(z,t)}{\partial t}. \qquad (2.2)$$

Equations (2.1) and (2.2) are the time-domain forms of the general transmission line equations, often referred to as the Telegrapher's Equations.
By differentiating equation (2.1) with respect to *z* and (2.2) with respect to *t*, we get

$$\frac{\partial^2 V(z,t)}{\partial z^2} = -R\frac{\partial I(z,t)}{\partial z} - L\frac{\partial^2 I(z,t)}{\partial t \partial z}. \qquad (2.3)$$

$$\frac{\partial^2 I(z,t)}{\partial t \partial z} = -G\frac{\partial V(z,t)}{\partial t} - C\frac{\partial^2 V(z,t)}{\partial t^2}. \qquad (2.4)$$

By putting equations (2.2) & (2.4) in (2.3), we get equation for line voltage *V(z,t):*

$$\frac{\partial^2 V(z,t)}{\partial z^2} = R\left(GV(z,t) + C\frac{\partial V(z,t)}{\partial t}\right) + L\left(G\frac{\partial V(z,t)}{\partial t} + C\frac{\partial^2 (z,t)}{\partial t^2}\right),$$

or

$$\frac{\partial^2 V(z,t)}{\partial z^2} - (RC + LG)\frac{\partial V(z,t)}{\partial t} - LC\frac{\partial^2 (z,t)}{\partial t^2} - RGV(z,t) = 0, \qquad (2.5)$$

The same expression can also be derived for current *I (z,t).*
Assuming a harmonic time dependence $e^{j\omega t}$ and denoting $V(z, t) = Re\{v(z)\, e^{j\omega t}\}$ and $I(z, t) = Re\{i(z)\, e^{j\omega t}\}$, where *Re* represents the real part of a complex quantity and ω represents the angular frequency of harmonic signal, equations (2.1) & (2.2) can be further simplified to

$$\frac{\partial v(z)}{\partial z} = -(R + j\omega L)i(z) \qquad (2.6)$$

$$\frac{\partial i(z)}{\partial z} = -(G + j\omega C)v(z) \qquad (2.7)$$

And voltage wave equation becomes:

$$\frac{\partial^2 v(z)}{\partial z^2} - (RG - \omega^2 LC)v(z) - j\omega(RC + LG)v(z) = 0 \qquad (2.8)$$

The general solution of equation (2.8) is

$$v(z) = v^+ e^{-\gamma z} + v^- e^{-\gamma z} \qquad (2.9)$$

where v^+ v^- are arbitrary amplitude constants for wave propagation in $+z$ and $-z$ directions respectively and γ is the complex propagation constant, which is function of frequency, its unit is [m^{-1}] and can be written as:

$$\gamma = \alpha + j\beta = \sqrt{(R + j\omega L)(G + j\omega C)} \tag{2.10}$$

Similarly, we can derive an equation for current wave on the transmission line which is given below,

$$i(z) = i^+ e^{-\gamma z} + i^- e^{-\gamma z} \tag{2.11}$$

By multiplying equation (2.9) with harmonic time dependence and taking the real part of that equation we can convert equation (2.9) in time domain form which is given below:

$$V(z,t) = \left|v_0{}^+\right| \cos(\omega t - \beta z + \Phi^+) e^{-\alpha z} + \left|v_0{}^-\right| \cos(\omega t + \beta z + \Phi^-) e^{\alpha z} \tag{2.12}$$

Where $\Phi^{\pm}$ is the phase angle of complex voltage $v^{\pm}=v_0{}^{\pm}e^{j\Phi\pm}$ and $e^{-\alpha z}$ represents the damping factor from which we can deduce that α represents the decay with distance z and is therefore called attenuation constant and measures in dB/m. β is phase constant of propagation wave and measures in rad/m or deg/m.
The phase velocity is the velocity of any point and can be calculated as:

$$v_p = \frac{dz}{dt} = \frac{d}{dt}\left(\frac{\omega t + \Phi^+ - const}{\beta}\right) = \frac{\omega}{\beta}. \tag{2.13}$$

The wavelength is the distance between two successive reference points on the wave with the same phase at a fixed instant of time and can be written as:

$$[\omega t - \beta z] - [\omega t - (z + \lambda)] = 2\pi, \tag{2.14}$$

or

$$\lambda = \frac{2\pi}{\beta} = \frac{2\pi v_p}{\omega} = \frac{v_p}{f}. \tag{2.15}$$

There is another important parameter which characterizes a transmission line called characteristics impedance Z_c, which relates the voltage wave to the corresponding current wave at any point of the line,

$$\frac{v^+}{i^+} = Z_c = \frac{-v^-}{i^-}. \tag{2.16}$$

Z_c can be canculated by inserting equation (2.9) into equation (2.6) which gives,

$$v(z) = \frac{R + j\omega L}{\gamma} i(z).$$

where

$$Z_c = \frac{R + j\omega L}{\gamma} = \sqrt{\frac{R + j\omega L}{G + j\omega C}}, \tag{2.17}$$

is the characteristics impedance of the transmission line.

2.2 Loss-Free Transmission line:

Loss free transmission line means a transmission line without dielectric losses and resistive losses in the conductor, i.e., R=G=0. The propagation constant for such a transmission line becomes (using equation (2.10))

$$\gamma = j\omega\sqrt{LC} \tag{2.18}$$

and characteristics impedance Z_c becomes pure real and using equation (2.17) it can be written as;

$$Z_c = \sqrt{\frac{L}{C}} \tag{2.19}$$

2.3 Low-Loss Transmission Line:

In practice all transmission lines are lossy but these losses are usually small; that is, $R << \omega L$ and $G << \omega C$. In many practical problems these losses can be neglected, but sometimes these losses become of interest (e.g. in case of measuring quality factor Q of a resonant cavity). We will see now how the low loss approximation simplifies the expressions for propagation constant and characteristics impedance.

The general expression for propagation constant can be given by equation (2.10);

$$\gamma = \alpha + j\beta = \sqrt{(R + j\omega L)(G + j\omega C)}$$

which can be further simplified as

$$\gamma = \sqrt{(j\omega L)(j\omega C)\left(1 + \frac{R}{j\omega L}\right)\left(1 + \frac{G}{j\omega C}\right)}$$

$$= j\omega\sqrt{LC}\sqrt{1 - j\left(\frac{R}{\omega L} + \frac{G}{\omega C}\right) - \frac{RG}{\omega^2 LC}}$$

Using low loss approximation $R << \omega L$ and $G << \omega C$ we can say that $RG << \omega^2 LC$ so above equation reduces to

$$\gamma = j\omega\sqrt{LC}\sqrt{1 - j\left(\frac{R}{\omega L} + \frac{G}{\omega C}\right)}$$

If we ignore the term $(R/\omega L+G/\omega C)$ in above equation then we get the same purely imaginary propagation constant as we have got for a lossless transmission line. So Taylor series expansion is used to obtain the first higher order real term for the propagation constant. So using Taylor series expansion we can write above equation as,

$$\gamma \approx j\omega\sqrt{LC}\left[1 - \frac{j}{2}\left(\frac{R}{\omega L} + \frac{G}{\omega C}\right)\right],$$

$$\approx j\omega\sqrt{LC} + \frac{1}{2}\left(\frac{R}{L} + \frac{G}{C}\right) = \alpha + j\beta. \qquad (2.20)$$

where

$$\beta \approx \omega\sqrt{LC} \qquad (2.21)$$

and

$$\alpha \approx \frac{1}{2}\left(\frac{R}{L}+\frac{G}{C}\right) \tag{2.22}$$

To the first order the characteristics impedance is still same as in the case of lossless transmission line so

$$Z_c \approx \sqrt{\frac{L}{C}}, \tag{2.23}$$

is the characteristics impedance for both, the low-loss and the lossless case.
Using equation (2.23) equation (2.22) can be written in terms of characteristics impedance Z_c as,

$$\alpha \approx \frac{1}{2}\left(R\sqrt{\frac{C}{L}}+G\sqrt{\frac{L}{C}}\right)=\frac{1}{2}(RY_c+GZ_c). \tag{2.24}$$

where $Y_c=1/Z_c$ is characteristics admittance of the transmission line.

2.4 Terminated Lossy Line and Scattering Matrices:

Now we will examine the properties of a transmission line having a characteristic impedance Z_c terminated with a load impedance Z_L at position z=0. Figure 2.2 illustrates schematically a transmission line terminated in a load impedance Z_L.

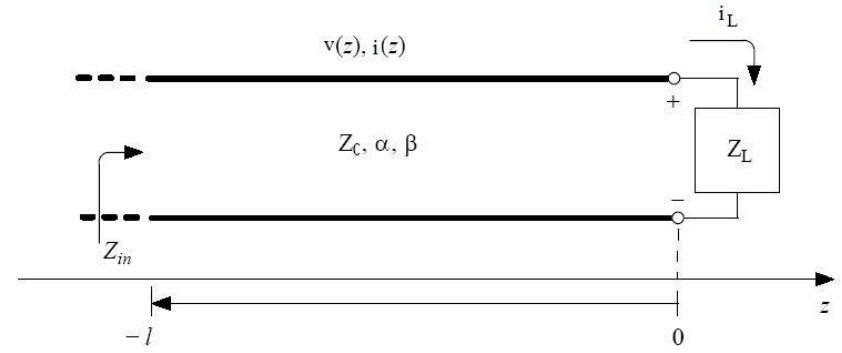

Figure 2.2 Terminated lossy transmission line

If $Z_L \neq Z_c$ the incident wave generated by the generator at $z < 0$ will be reflected at the interference between the line and the load. The presence of reflected wave leads to standing waves on the transmission line.

At any point on the transmission line, total voltage can be written as a sum of an incident wave and reflected wave:

$$v(z) = v^{+}e^{-\gamma z} + v^{-}e^{-\gamma z}. \tag{2.25}$$

Similarly the current at any point on the line can be written as:

$$i(z) = i^{+}e^{-\gamma z} + i^{-}e^{-\gamma z}.$$

Using equation (2.16) above equation can be written as:

$$i(z) = \frac{v^{+}}{Z_c}e^{-\gamma z} - \frac{v^{-}}{Z_c}e^{\gamma z}. \tag{2.26}$$

The load impedance at $z=0$ can be obtained by putting $z=0$ in equations (2.25) & (2.26) and dividing them:

$$Z_L = \frac{v(0)}{i(0)} = \frac{v^{+} + v^{-}}{v^{+} - v^{-}}Z_c. \tag{2.27}$$

Using above equation the relation between incident and reflected wave can be written as:

$$\Gamma_L = \frac{v^{-}}{v^{+}} = \frac{Z_L - Z_c}{Z_L + Z_c}, \tag{2.28}$$

where Γ_L is called the reflection coefficient of the load. If the load impedance is equal to the characteristics impedance $Z_L = Z_c$ then there in no reflected wave and $\Gamma_L = 0$. If the load impedance is zero (short circuit) or infinite (open circuit) all of the voltage is reflected and the value of reflection coefficient becomes -1 and 1 respectively. The minus sign shows the reflected wave is 180 out of phase with the incident wave.
At any other point at distance l toward the generator, the reflection coefficient is given as:

$$\Gamma_L(l) = \frac{v^{-}e^{-\gamma l}}{v^{+}e^{\gamma l}} = \Gamma_L e^{-2\gamma l} \tag{2.29}$$

The voltage and current on the transmission line in terms of Γ_L can be written as:

$$v(z) = v^{+}(e^{-\gamma z} + \Gamma e^{\gamma z}) \tag{2.30}$$

$$i(z) = \frac{v^+}{Z_c}(e^{-\gamma z} - \Gamma e^{\gamma z}) \tag{2.31}$$

The input impedance Z_{in} seen by the source can be obtained by putting $z=-l$ in equations (2.30) & (2.31) and dividing them. So,

$$Z_{in} = \frac{v(-l)}{i(-l)} = Z_c \frac{1+\Gamma_L e^{-2\gamma l}}{1-\Gamma_L e^{-2\gamma l}} = Z_c \frac{Z_L + Z_c \tanh(\gamma l)}{Z_c + Z_L \tanh(\gamma l)}, \tag{2.32}$$

Equation (2.32) is an important relation which relates the characteristics impedance to the any load impedance and called the transmission line impedance equation.
The input impedance for a lossless transmission line can easily be obtained by putting $\gamma=j\beta$ in equation (2.31), as for a lossless transmission line we have $\alpha=0$.
To analyze the effects of an obstacle along the transmission line, the scattering matrix formulation is used. In this case incident voltage v_1^+ and v_2^+ are assumed to be each side of the obstacle see figure (2.3). The relation between incident and outgoing waves v_1^-, v_2^- is given by scattering matrix S

$$\begin{pmatrix} v_1^- \\ v_2^- \end{pmatrix} = \begin{pmatrix} S_{11} S_{12} \\ S_{21} S_{22} \end{pmatrix} \begin{pmatrix} v_1^+ \\ v_2^+ \end{pmatrix}. \tag{2.33}$$

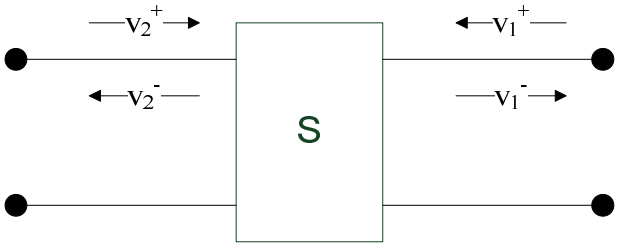

Figure 2.3 An obstacle on a transmission line characterizng by a scattering metric S

Chapter 3

Coplanar Waveguides (CPW) Transmission Lines

Coplanar waveguides (CPW) proposed by C. P. Wen in 1969 [13] are chosen to study the properties of different dielectrics for this thesis for its easy fabrication as compared to the other transmission lines like microstrip line because CPWs have a simple layer structure with no need for deposition of any insulating layer. The most significant advantage that a CPW has over a microstrip line is that active and passive components can be connected in shunt from the conducting strip to the ground plane on the same side of the substrate. In a microstrip line connection to the ground plane is made by drilling a hole through the substrate which is somehow difficult for ceramic materials such as alumina. Another advantage is that the characteristic impedance is directly related to the ratio of the width of the central strip to the width of gap between the ground plane and the central strip, so it is possible to design various geometries for certain dielectric substrate easily. Furthermore, a CPW has a very small radiation loss which may influence the quality factor of the resonator. There are two classifications of the CPW transmission, one is conventional CPW which consists of a center strip conductor with semi-infinite ground planes on each side (figure 3.1) and the other one is conductor backed CPW with an additional ground plane at the bottom surface of the substrate.

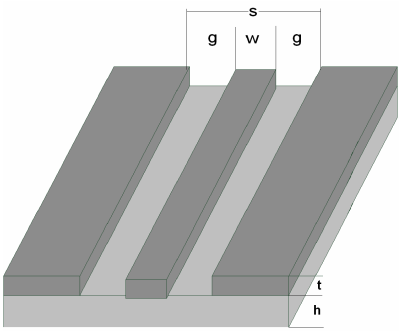

Figure 3.1 A cross sectional view of conventional CPW. A central conductor strip and two ground planes are placed on some dielectric substrate.

In the following different characteristics of conventional CPW, we used in this work, are described below.

3.1 Characteristics Impedance Z_c:

The characteristics impedance of CPW depends on its geometry (figure 3.2) and is given as [14]:

$$Z_c = \frac{60\pi}{\sqrt{\varepsilon_{eff}}\left(\frac{K(k_1)}{K(k_1^{'})} + \frac{K(k_2)}{K(k_2^{'})}\right)}, \tag{3.1}$$

where ε_{eff} is the effective dielectric constant of the dielectric is given as:

$$\varepsilon_{eff} = \frac{1+\varepsilon_r \hat{K}}{1+\hat{K}}, \tag{3.2}$$

where

$$\hat{K} = \frac{K(k_1^{'})K(k_2)}{K(k_1)K(k_2^{'})}, \tag{3.3}$$

where K is the complete elliptical integral of first kind, ε_r is the relative dielectric constant of substrate and

$$k_1 = \frac{w}{s}, \tag{3.4}$$

$$k_2 = \frac{\sinh(\frac{\pi w}{4h})}{\sinh(\frac{\pi s}{4h})}, \tag{3.5}$$

$$k_1^{'} = \sqrt{1-k_1^{2}}, \tag{3.6}$$

$$k_2' = \sqrt{1 - k_2^2}, \qquad (3.7)$$

where h is height of the substrate, w is width of central conductor, g is gap width and $s=2g+w$ as shown in figure 3.1.

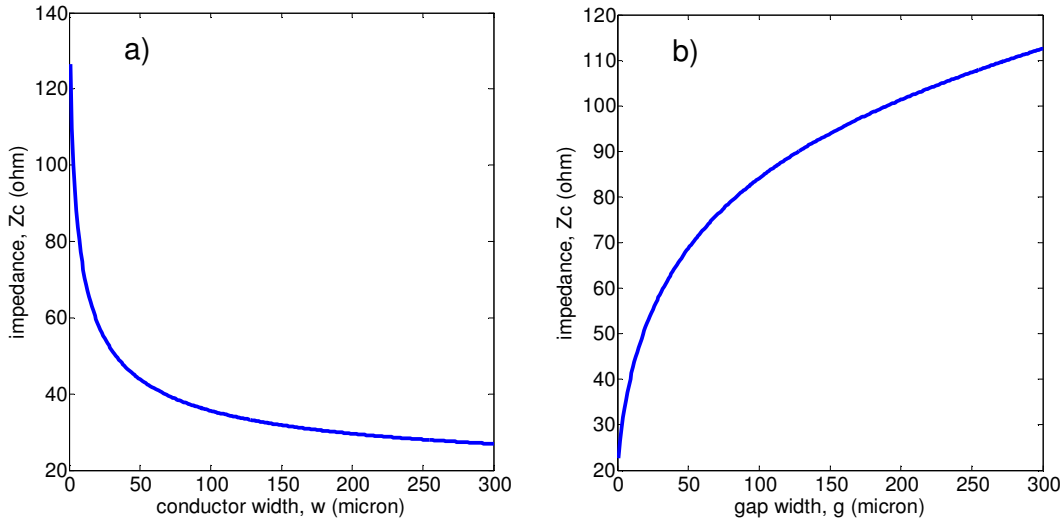

Figure 3.2 Dependance of the Characteristic impedance, Z_c (Ω), for CPW geometry assuming MgO as dielectric with ε_r =11.1. a) Plot of the characteristic impedance vs central conductor width, w assuming height of substrate, h=500μm and gap width, g=16μm b) Plot of characteristic impedance vs gap width, g assuming height of substrate, h=500μm and central conductor width, w=37.6μm

3.2 Attenuation:

In general the electric field E of a wave traveling along a transmission line in z direction with angular frequency ω can be written as:

$$E = E_0 e^{i(\omega t - \gamma z)},$$

where $\gamma=\alpha+i\beta$ is the propagation constant with β the phase constant (imaginary part) and α the attenuation constant (real part)[for detail see chapter 2]. Several loss sources contribute to the attenuation of a CPW per unit length.

$$\alpha = \alpha_d + \alpha_c + \alpha_s + \alpha_r \qquad (3.8)$$

where α_d represents the attenuation due to dielectric losses, α_c represents the attenuation due to conductor losses, α_s and α_r represent the attenuation due to scattering losses and

radiative losses respectively which can be neglected in the frequency regimes of interest. So we will discuss here only attenuation constants due to dielectric and conductor losses.

Dielectric Losses:

The attenuation due to dielectric losses α_d can be given as[14]:

$$\alpha_d = \frac{\omega \varepsilon_r}{2c_0\sqrt{\varepsilon_{eff}}} q \tan\delta_e, Nepers/meter \qquad (3.9)$$

where neper[1] is logarithmic unit of ratio, ε_r is the relative permittivity of the dielectric, $\tan\delta_e$ is the dielectric loss tangent, ε_{eff} is the effective dielectric constant defined in equation (3.2) ω is angular frequency, c_0 is speed of light in vacuum and q is the filling factor which can be defined in terms of ε_{eff} and ε_r as:

$$q = \frac{\varepsilon_{eff} - 1}{\varepsilon_r - 1} \qquad (3.10)$$

Table 3.1 shows the attenuation constants due to the MgO and LAO.

Dielectric	ε_r	Loss tangent $\tan\delta_e$	Attention α_d
MgO	11.1	$6.2\ 10^{-6}$@ 10GHz 77K [16]	0.0022
LAO	23.5	0.00003@ 5GHz, 77K [15]	0.0053
		$7.6\ 10^{-6}$@ 10GHz 77K [16]	0.0027

Table 3.1 Dielectric losses for MgO and LAO

Conductor Losses:

The attenuation constant due conductor losses of a superconducting CPW can be written as [14]:

$$\alpha_c = \frac{R_{sm} b^2}{16 Z_c K^2(k_1)[b^2 - a^2]}\left[\frac{1}{a}\ln\left\{\frac{2a(b-a)}{\Delta(b+a)} + \frac{1}{b}\ln\left(\frac{2b(b-a)}{\Delta(b+a)}\right)\right\}\right], \qquad (3.11)$$

[1] Neper (Np) is just like a decibel (dB). The difference between the decibel and the neper is that in the decibel we use base-10 logarithms to compute where in neper we use base-e=2.718 to compute ratios i.e. $Np=\ln(x_1/x_2)$ where x_1 and x_2 are the values of interest.

where $a=w/2$, $b=s/2$, Δ is stopping distance[2] and R_{sm} is modified surface impedance of superconducting film of thickness t which is given as:

$$R_{sm} = \mu_0 \omega t \, \mathrm{Im}\left(\frac{\cot(k_c t) + \csc(k_c t)}{k_c t} \right). \tag{3.12}$$

The complex wave number k_c in the superconductor at a frequency ω is given as:

$$k_c = \left(\frac{1}{\lambda_L} \right)^2 + 2i \left(\frac{1}{\delta_{skin}} \right), \tag{3.13}$$

where λ_L and δ_{skin} are London penetration depth and skin depth of superconductor respectively and given as:

$$\lambda_L = \sqrt{\frac{1}{\omega \mu_0 \sigma_s}}$$

$$\delta_{skin} = \sqrt{\frac{2}{\omega \mu_0 \sigma_n}}$$

where σ_n and σ_s are the real and imaginary parts of the complex conductivity, $\sigma=\sigma_n-i\sigma_s$, μ_0 is the permeability of the free space and ω is the angular frequency.

3.3 Kinetic Inductance:

The total inductance per unit length L_{tot} of the CPW is composed of external inductance L_{ext} and kinetic inductance L_{kin} caused by cooper pairs due to their inertia.

$$L_{tot} = L_{ext} + L_{kin}. \tag{3.14}$$

The external inductance per unit length can b written as[14]:

[2] The CPW attenuation constant is derived by the modified matched asymptotic expansion technique where an approximate current density is first assumed on CPW conductors and an equation for CPW attenuation is derived. This equation involves a contour integral. Instead of evaluating this integral out to the edge of conductors where the fields are singular, the limits of integral are taken at some distance just before the edges. This short length before the edges is called stopping distance. Stopping distances for different films thickness, t are given in the reference [14]. For a 120nm film thickness and 94nm of London penetration depth the stopping distance is about 4nm-6nm.

$$L_{ext} = \frac{\mu_0 K(k_1')}{4K(k_1)}, \tag{3.15}$$

where μ_0 is the permeability of free space and K is the elliptical integral of first kind and k_1 and k_1' are defined in equations (3.4) and (3.6) respectively.
The kinetic inductance also depends on the geometry of CPW and the London penetration depth and can be written as[17]:

$$L_{kin} = \mu_0 \lambda_L(T) \frac{C}{4ADK(k_1)} \left(\frac{1.7}{\sinh[t/2\lambda_L(T)]} + \frac{0.4}{\sqrt{[(B/A)^2 - 1][1-(B/D)^2]}} \right), \tag{3.16}$$

where t is thickness of film (fig. 3.1), $\lambda_L(T)$ is London penetration depth as a function of temperature T and the parameters A through D are given below:

$$A = -\frac{t}{\pi} + \frac{1}{2}\sqrt{\left(\frac{2t}{\pi}\right)^2 + w^2},$$

$$B = \frac{w^2}{4A},$$

$$C = B - \frac{t}{\pi} + \sqrt{\left(\frac{t}{\pi}\right)^2 + \frac{1}{4}(s-w)^2},$$

$$D = \frac{2t}{\pi} + C.$$

The London penetration depth as a function of temperature according to the two-fluid model can be written as[18]:

$$\lambda_L(T) = \frac{\lambda(0)}{\sqrt{1-\left(\frac{T}{T_c}\right)^4}}, \tag{3.17}$$

where $\lambda_L(0)$ is the London penetration depth at 0K and T_c is the critical temperature of film.

3.4 Microwave Resonators:

A resonator is an object which stores energy and transforms it from kinetic energy to potential energy and vice versa with a constant rate ω, which is called resonance frequency of the resonator. There are large varieties of resonators such as mechanical resonators, photons trapped inside an optical cavity and electrical circuits consisting of capacitors and inductors. In the case of electrical circuits the energy stored in inductors plays a role of potential energy and energy stored in capacitors plays a role of kinetic energy.

A. Wallraff, in reference [19], showed that a superconducting two levels system, playing a role of an artificial atom, can strongly coupled to an on-chip cavity consisting of superconducting CPW resonator. This kind of structure—artificial atom-resonator system— has great prospects both for performing quantum computations and quantum optics experiments in solids.

Distributed elements such as pieces of transmission line are used to get a high quality factor resonator. In such kinds of resonators the electrical and magnetic energies are stored in the same regions of resonator unlike in lumped elements resonant circuits where the electrical and magnetic energies are stored in different spatial regions of the resonator.

In the previous chapter we have seen if there is a mismatch between a load impedance and characteristics impedance of a transmission line then reflection occurs from the load as shown in equation (2.28). And if the input signal is a continuous ac signal then the reflected waves mix with incoming waves and produce standing waves. In case of short circuit load (Z_L=0, the case we have used in this work) the signal is completely reflected from the load and the standing waves fulfill the boundary conditions at the short and open end. In case of quarter wave length resonator, where the resonator is opened at one end and shorted to the ground at the other end (figure 3.3), only odd multiple of quarter wavelength, $\lambda/4$, can fulfill the different boundary conditions. The magnetic field is zero and the electric field is maximum at the open end and opposite of this occurs at the short end as shown in figure 3.3. For a given length, l the resonance frequencies for these types of resonators are given below:

$$f_n = n\frac{v_{ph}}{4l}. \qquad (3.18)$$

v_{ph} is phase velocity of ac signal and can be given as:

$$v_{ph} = \frac{c_0}{\sqrt{\varepsilon_{eff}}}, \qquad (3.19)$$

where ε_{eff} is effective dielectric constant of the substrate and c_0 is speed of light in vacuum.

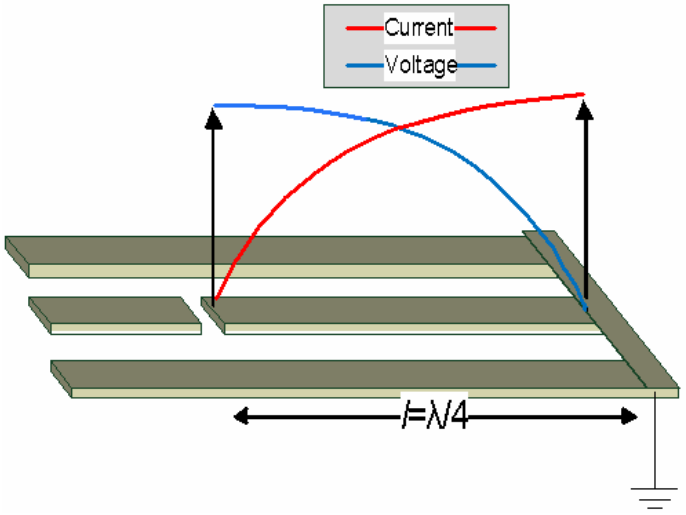

Figure 3.3 Illustration of quarter wavelength CPW resonator.

The quality factor, Q of a resonator is of high interest in quantum computation applications. It indicates how good a resonator is at storing energy and influences the rate of measurement in qubit experiments and is given by:

Q=Energy stored /energy dissipated per cycle

If the energy is dissipated through more than one source then one can define a Q value for each source contribution and the total Q value is defined then

$$\frac{1}{Q_{tot}} = \left(\frac{1}{Q_1} + \frac{1}{Q_2} + \frac{1}{Q_3} ..... \frac{1}{Q_N} \right). \tag{3.20}$$

Normally there are two main contributions in the total Q value, one contribution is from internal losses which include resistive losses and dielectric losses and the other contribution is from external losses which include the losses due to the coupling of the resonator via capacitors with the outside world. Believing those two as main sources of dissipation one can defined total factor as:

$$\frac{1}{Q_{tot}} = \frac{1}{Q_{\text{int}}} + \frac{1}{Q_{ext}}. \tag{3.21}$$

There are three possible regimes for a resonator, one is the undercoupled regime, the second is the overcoupled regime and the third is the critical coupled regime. If the total quality factor is dominated by internal quality factor Q_{int} then the resonator is said to be in the undercoupled regime, if the total quality factor is dominated by external quality factor Q_{ext} then the resonator is said to be in overcoupled regime. And if the external

quality factor Q_{ext} and the internal quality Q_{int} factor is same the resonator is said to be in the critical coupled regime.
Rate of measurement is determined by the decay rate of a photon in the cavity which is given as:

$$\kappa = \frac{f_0}{Q_{tot}}, \tag{3.22}$$

where f_0 is resonance frequency of the resonator.
The measurement rate should be faster than the decay rate of the qubit.

Chapter 4

Design Fabrication and Measurement Techniques

In this chapter the design, fabrication and measurements techniques of the superconducting CPW transmission lines are described. The characteristic impedance of a CPW transmission line depends on its geometry and dielectric constant of the substrate (for detail see chapter 3). In this thesis we used MgO as dielectric substrate, which is suitable for epitexial growth of YBCO, having relative dielectric constant of a 11.1. We also made resonator on MgO with a thin layer of STO atop and we will call it MgO/STO combination in the rest of the work. We want characteristic impedance of 50Ω to match the resonator structures with other coaxial cables and other microwave equipment to avoid reflections. The fabrication steps and measurements techniques of the resonators are described below.

4.1 Design of CPW Transmission Line:

First thing we need to decide about resonators is its resonance frequency which depends on its length. In quantum application this resonance frequency becomes a very important parameter because to be in zero temperature limit we need resonance frequencies much higher than 1GHz such that the energy of microwave photon is much greater than thermal photons in the resonator ($hf >> k_B T$ where 1GHz~50mK) at millikelvin temperatures.
The length of a quarter wavelength resonator is obtained as:

$$l = \frac{c}{4\sqrt{\varepsilon_{eff}}\, f_0} \qquad (4.1)$$

where c is the speed of light in vacuum, f_0 is the resonance frequency and ε_{eff} is the effective dielectric constant of the substrate (equation 3.2). To calculate the characteristics impedance and effective dielectric constant I wrote a program in Matlab (Appendix). The input parameters are the central conductor width, height of the substrate and the relative dielectric constant. Figure 4.1 shows the characteristics impedance for different gap width, g, for a MgO of height of 500μm.

Substrate Material	Resonance frequency f_0 (GHz)	Effective dielectric constant ε_{eff}	Length of resonator l (mm)	Center conductor width w (μm)	Gap width g (μm)
MgO	6.4	6.06	4.8	37.6	16

Table 4.1 Geometry of resonators fabricated on MgO

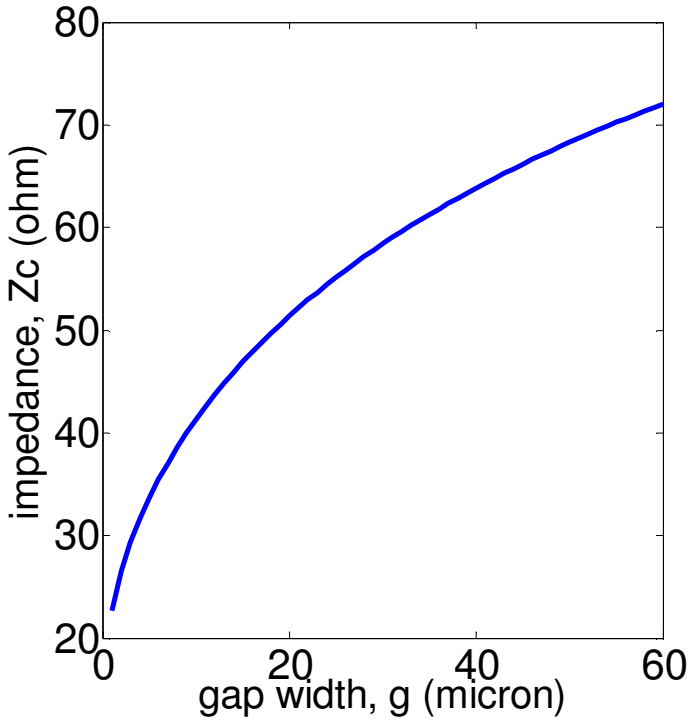

Figure 4.1 Characteristic impedance vs gap width, g for a center conductor width of 37.6μm. We need 16 μm of gap width to get 50Ω characteristic impedance.

To connect the resonator with the outside world we need a coupling capacitor having certain coupling capacitance C_c at the input and output. For λ/4 resonator only one coupling capacitor at the input is used while the other end of the resonator is shorted to ground. Introducing a coupling capacitor at the input allows leakage of energy from the resonator and hence determines the external quality factor Q_{ext}. The external quality factor of a quarter wavelength resonator consisting of a capacitance $C_r=Cl/2$, where C is the capacitance per unit length and l is the length of resonator which is coupled to a load resistance R through a coupling capacitance C_c is given as [20]:

$$Q_{ext} = \frac{[1+(\omega_0 C_c R)^2][C_r + C_c]}{\omega_0 C_c^{\,2} R}, \qquad (4.2)$$

where $\omega_0=2\pi f_0$ is the resonance frequency of the resonator. Figure 4.2 shows how the external quality factor decreases with increasing value of the coupling capacitance.

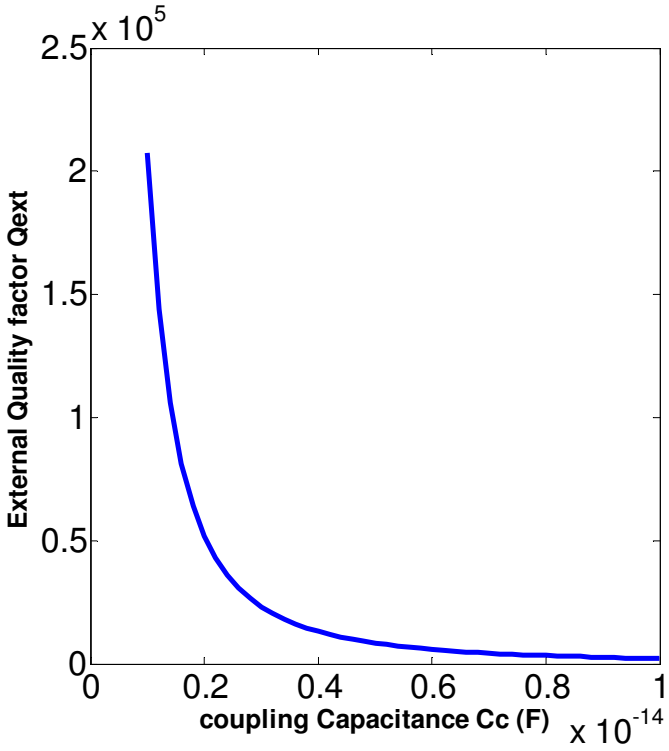

Figure 4.2 Plot of external quality factor Q_{ext} vs coupling Capacitance C_c

There are several ways these coupling capacitors can be designed. In this work we designed interdigitated coupling capacitors with one finger on each side as shown in figure 4.3. For a certain capacitance value the width, length and spacing of the fingers are obtained using Microwave Office software.

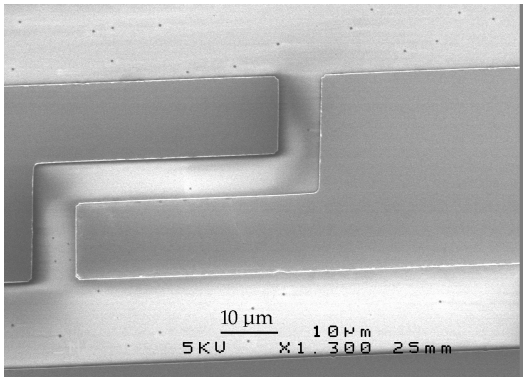

Figure 4.3 Interdigitated capacitor with one finger on each side.

We designed two capacitors with different coupling capacitances on the MgO and one resonator on MgO/STO combination. Table 4.2 shows the different parameters of coupling capacitors and corresponding external quality factors of the resonators fabricated on MgO and MgO/STO.

Substrate	Length µm	Width µm	Spacing µm	Capacitance C_c (fF)	Q_{ext}
MgO Resonator 1	45	15	7.6	4.15	$1.2\ 10^4$
MgO Resonator 2	35	15	7.6	3.31	$2.0\ 10^4$
MgO/STO Resonator 3	35	15	7.6	3.31	$2.0\ 10^4$

Table 4.2 Geometry of Coupling capacitors and corresponding External Quality factor

4.2 Fabrication of CPW Transmission Line:

All resonators are fabricated in the clean-room of the nanofabrication laboratory at MC2 department of Chalmers University of Technology. Before fabricating the resonators two optical masks, one for MgO and other for LAO, are made using e-beam lithography and lift off techniques. The design of these masks is made in AutoCAD for 5×5mm chips.
In the following the different steps involved in fabrication are described.

Substrate Cleaning:

Before doing any kind of deposition the substrates are cleaned in acetone and isopropanol.

Depositing Niobium:

After cleaning the substrates niobium films of 120nm thickness are sputtered. The sputtering is done with following parameters:

- Process pressure: 1.10^{-2}mbar
- Argon flow rate: 25sccm
- Power: 100W

In case of MgO/STO combination a thin layer of STO (40nm-50nm) was deposited using Pulse Laser Deposition (PLD) technique before depositing the niobium.

Spinning the Resist:

After sputtering the niobium film a layer of S1813 positive photo resist is spun at 6000rpm for 1.5min. The photo resist is then baked for 5min at 90^{o}C to improve the adhesion of the resist.

Deep Ultra-Violet (DUV) Exposure and Developing:

To expose the resist a **KS MJB3-DUV 248nm** mask aligner is used and the exposed areas are then removed in MF-319 developer. Before exposing and developing the resonator structure, a square mask is used to remove the resist from the edges because at edges normally there is thick resist which may create problems in aligning the substrate. The exposure time for the edges is 200sec and the developing time is 25sec in MF-319 developer. After this the resonator structure is patterned with 90sec exposure time and 25sec developing time in the same developer. The samples were always checked under the microscope to make sure that all structures were developed completely.

Etching and Ashing:

The next step is to mill away the uncovered part of the sample. This is done by using **Argon Ion Beam Milling System (CAIBE Oxford Ionfab).** Different parameters are given below:

Base pressure: ~ 2 10^{-7} mbar
Process pressure: 2.3 10^{-4} mbar
Beam current: 7mA
Beam voltage: 300V

To calculate the etching rate of niobium for the parameters mentioned above, a test sample partially covered with photo resist was made. Then this sample was etched in the Ion milling machine for 30min then using AFM scans we calculated the etching rate of niobium. To etch the 120nm thick niobium film we needed to etch the sample for 85mins. But we etched our samples more than 100min just to make sure that there is no niobium

left in the gaps. In the case of MgO/STO combination we etched the sample for more than 100min just to make sure that also there is no STO left in the gaps.
After etching, the resist was removed by dipping the sample in acetone at 50°C for 20-30mins. At the end Reactive Ion Etching (RIE) is used for ashing in order to clean the sample and to remove the resist if there was some left.
Figure 4.4 represents the different fabrication steps schematically.

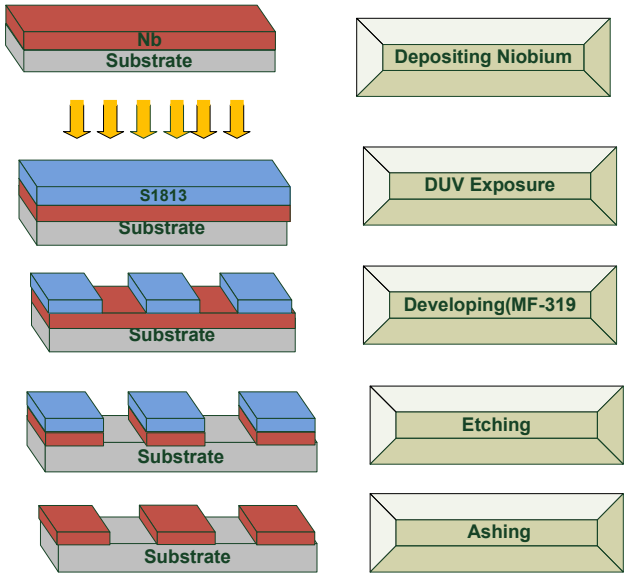

Figure 4.4 Schematically representation of different fabrication steps

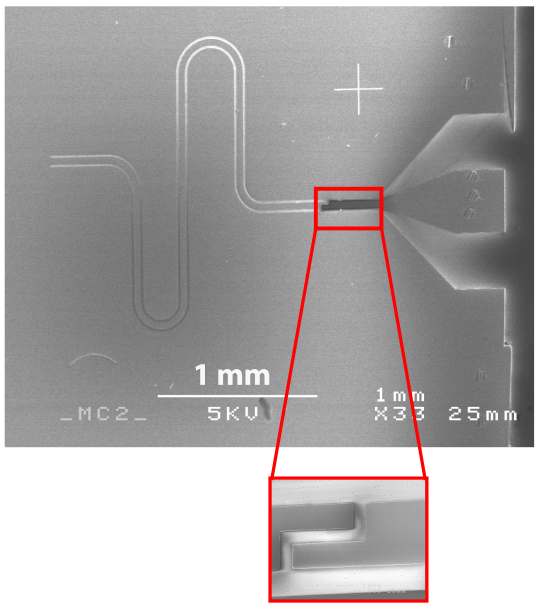

Figure 4.5 SEM picture of the resonator

4.3 Measurements Techniques:

Cryostat:

All the samples were measured in an Oxford Instruments HelioxVL system, a ^{3}He charcoal-absorber based cryostat capable of reaching temperatures below 300mK. Temperature of 4.2K can be obtained by dipping the stick into the ^{4}He dewar which contains μ-metal and superconducting magnetic shield. The whole system is located into an electromagnetic shielded room. The working principle of the HelioxVL system can be seen in reference [21].

Microwave Setup:

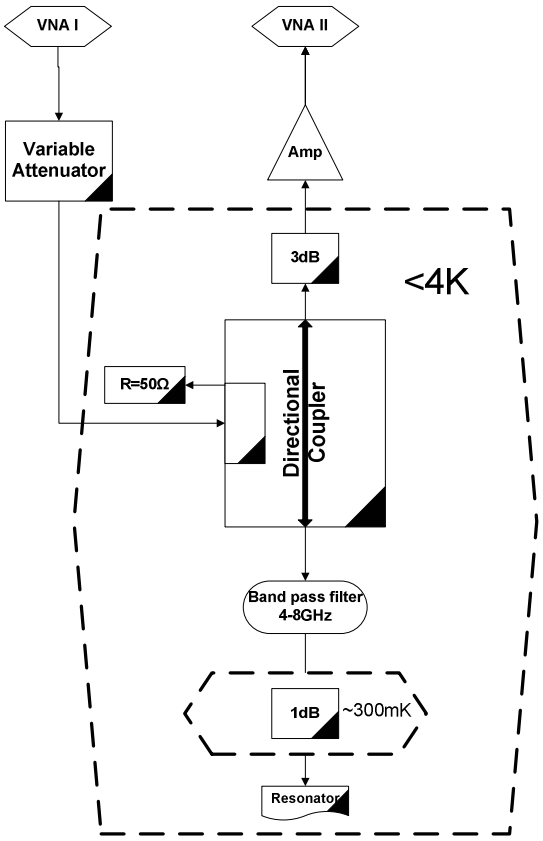

Figure 4.6 Microwave setup installed in the Cryostat

Figure 4.6 shows the microwave setup installed in the cryostat. VNA I shows the input port of vector network analyzer which goes to a variable attenuator. This variable attenuator goes to a directional coupler having coupling of 30dB and directivity of 20dB. The signal from directional coupler passes to a band pass filter and goes to the shorted resonator through a 1dB attenuator which is used to thermalize the coaxial cable at 1K. The signal is reflected from the resonator and goes to the output port of the vector network analyzer VNA II through an amplifier. The 3dB attenuator is used to reduce the noise coming from the amplitude going down to the resonator.

Chapter 5

Results and Discussion

The goal of this thesis work is to find out the dielectric losses of substrate suitable for epitaxial growth of YBCO at high frequencies (5-10GHz) and at milikelvin temperatures which will be very valuable for qubit applications (detail is given in chapter 1). We used Superconducting CPW resonator fabricated on MgO and LAO to find out the losses of these dielectrics. By measuring the total quality factor of the resonator we can easily extract the internal quality factor which is mainly limited by the losses due to the dielectrics. Information about the London penetration depth, λ_L and critical temperature of niobium films is obtained from the temperature dependent measurements of the resonance frequencies. Keeping the future work in mind we also tried to understand how a thin film of STO deposited on a MgO substrate affects our resonators. In the following we present the measurements results of different samples.

5.1 Resonators on MgO substrate:

There are two resonators fabricated on the MgO substrate one with larger coupling capacitance, **Resonator 1**, and the other with smaller coupling capacitance, **Resonator 2**. To measure the reflection coefficient S_{11} a Vector Network Analyzer (VNA) was used. By sweeping the probe signal over a frequency range the resonance peak can easily be detected either in the phase or magnitude of the reflected signal. On resonance the power transferred to the CPW resonator is maximum so the S_{11} curve should have a dip at the resonance. Typical S_{11} measurement curves in magnitude and phase are shown in figure 5.1(a) and 5.2(b) respectively.

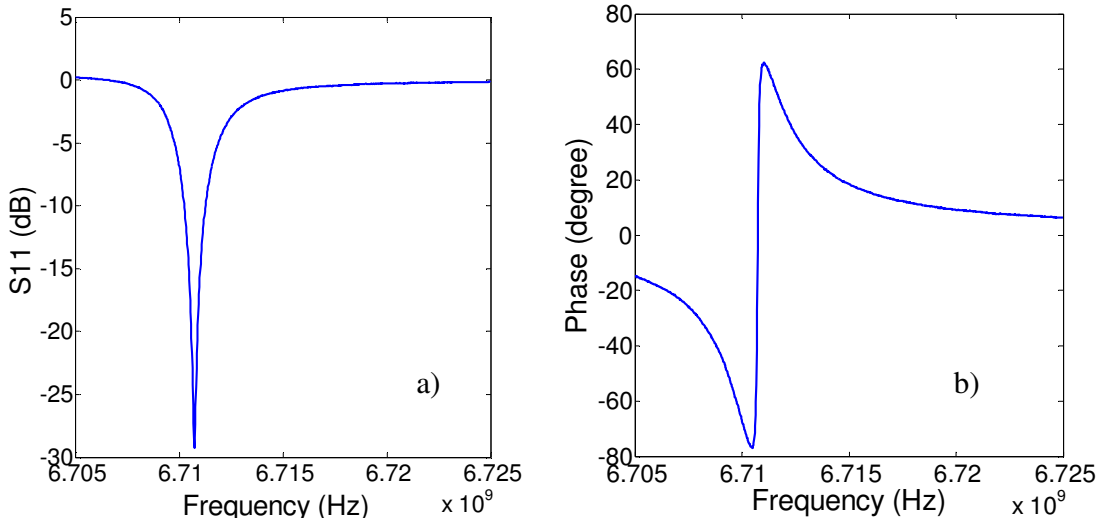

Figure 5.1 Measured S_{11} for CPW resonator (a) the magnitude response (b) the phase response

From the amplitude curve (figure 5.1 a) the total quality factor can be obtained as:

$$Q_{tot} = \frac{f_0}{\delta f} \tag{5.1}$$

where δf is the Full Width at Half Maximum (FWHM) of the resonance peak and f_0 is the resonance frequency which is the frequency corresponds to the minimum of reflection coefficient S_{11} as shown in figure 5.1 (a). The FWHM can be obtained by fitting the reflection coefficient of the resonators as shown in figure 5.2. The reflection coefficient of the resonator can be written as [20]:

$$\Gamma_r = s_{11} + \frac{s_{12}s_{21}\Gamma_s e^{-\gamma l}}{1 - s_{22}\Gamma_s e^{-2\gamma l}}, \tag{5.2}$$

where s_{ij} are the scattering parameters of coupling capacitor given in equation (5.3) & (5.4), Γ_s is reflection coefficient for the other end of the resonator and γ is the propagation constant of transmission line given in equation (2.20) for the low-loss transmission line. We set Γ_s=-1 for short circuit at the other end of the resonator.

$$s_{11} = s_{22} = \frac{1}{2iZ_c\omega C_c + 1}, \tag{5.3}$$

$$s_{12} = s_{21} = \frac{2iZ_c\omega C_c}{2iZ_c\omega C_c + 1}, \tag{5.4}$$

where Z_c is the characteristic impedance of CPW resonator, C_c is the coupling capacitance, ω is the angular resonance frequency of CPW resonator.

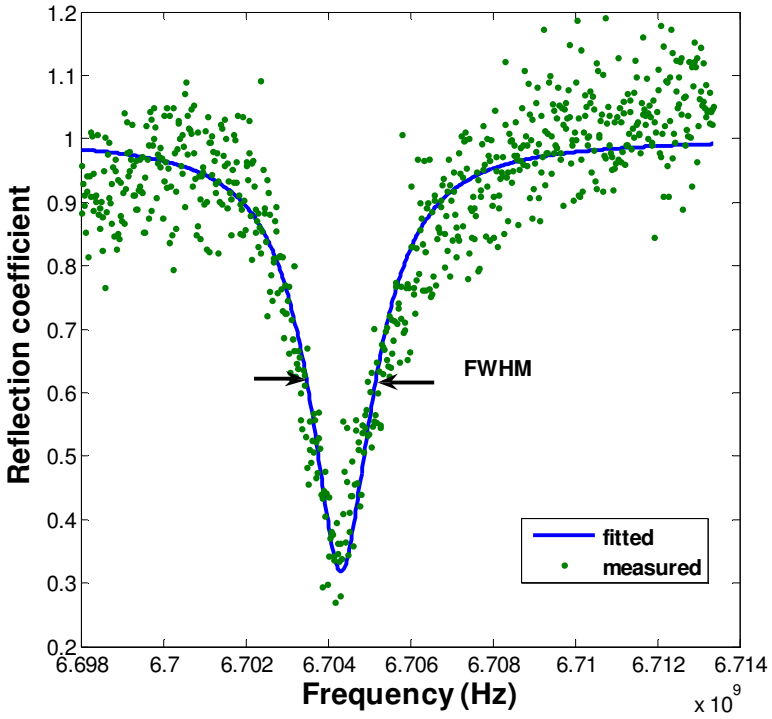

Figure 5.2 Measured magnitude response at low power for Resonator 1 on MgO (dots). The solid line is the fit of reflection coefficient Γ_r.

In the fitting curve we need to fit the coupling capacitance and from that value we can calculate the external quality factor, Q_{ext} using equation 4.2. We can also find the external quality factor when the resonator is in the critical coupled regime where the external and internal quality factors are same. Figure 5.3 shows the response of a resonator in polar coordinates (blue circle). The radius of circles represents the magnitude and the lines making the angles with horizontal line represent the phase of reflected signal. When the resonator is in the critical coupled regime the blue circle passes through the center. Each point of the data represents a different frequency of the probe signal and the point at extreme left represents the resonance frequency of the probe signal. By measuring the resonator response at different powers and temperatures we can find where the resonator is in critical coupled regime.

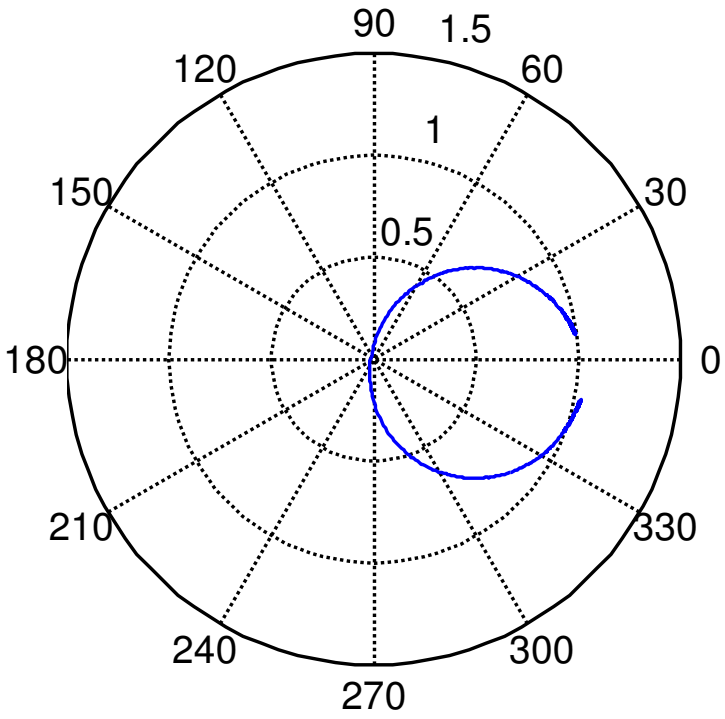

Figure 5.3 Response of resonator in polar form

Table 5.1 shows the external quality factors of the resonators on MgO.

Identity	Designed	From fitting	Polar plot
Resonator1	$1.2\ 10^4$	$7.11\ 10^3$	$7.067\ 10^3$
Resonator2	$2.0\ 10^4$	$4.7\ 10^3$	$7.14\ 10^3$

Table 5.1 The designed and measured external quality factors of the resonators on MgO

For the resonator 2 the external quality factor measured from fitting is different from what we measured from polar plot. One reason could be is that the impedance R (in equation 4.2) through which the capacitors is coupled to the resonator is not exactly 50Ω. But the value of external quality factor we got from polar plot is independent of R so we believe on that value.

We took the measurements at various power values from -110dBm to -30dBm at temperature of 300mK. At low powers the **Resonator1** was undercoupled and as we increased the power a transition from undercoupled to overcoupled regime was found but the **Resonator 2** is overcoupled at all values of power as shown in figure 5.4 & figure 5.5.

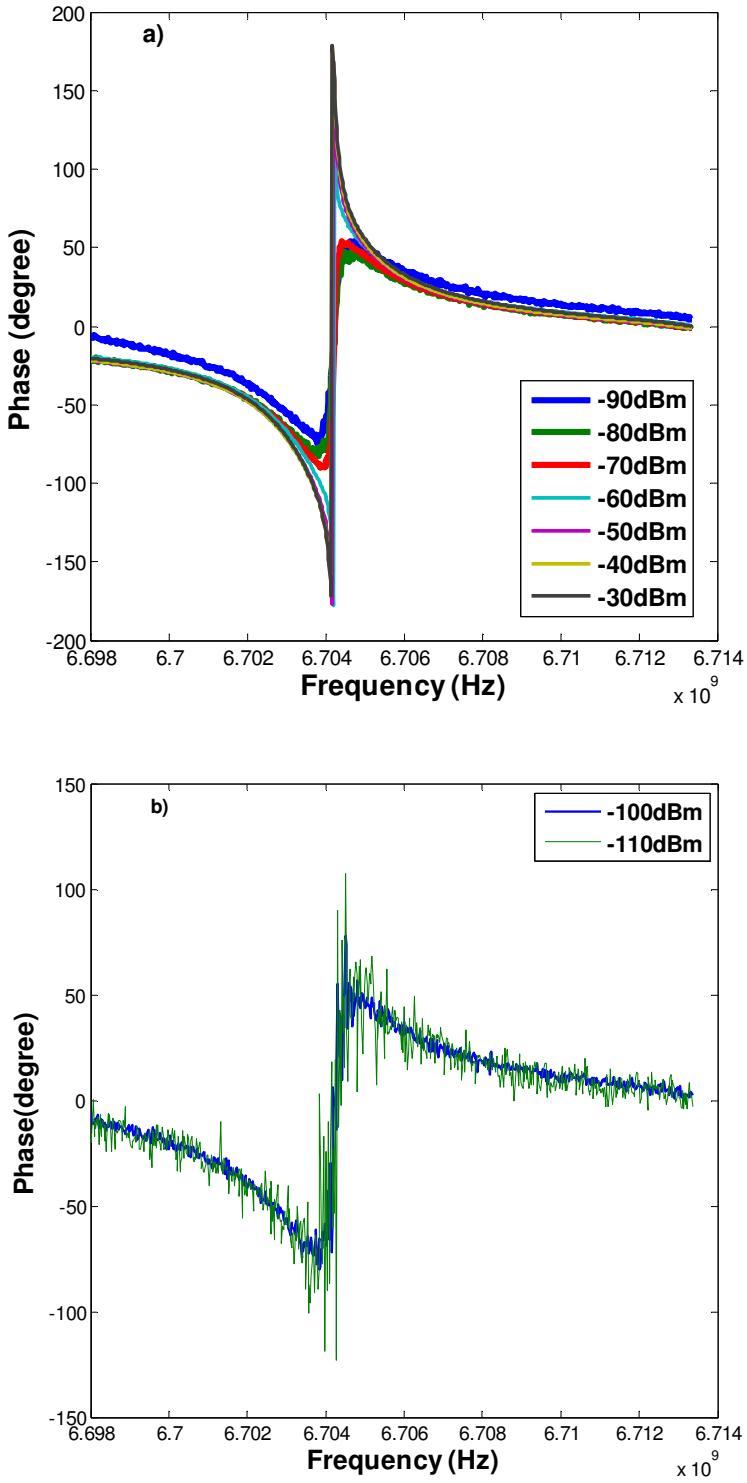

Figure 5.4 Phase response of the Resonator 1 at 300mK for different powers a) from -90dBm to -30dBm b) for -110dBm and -100dBm

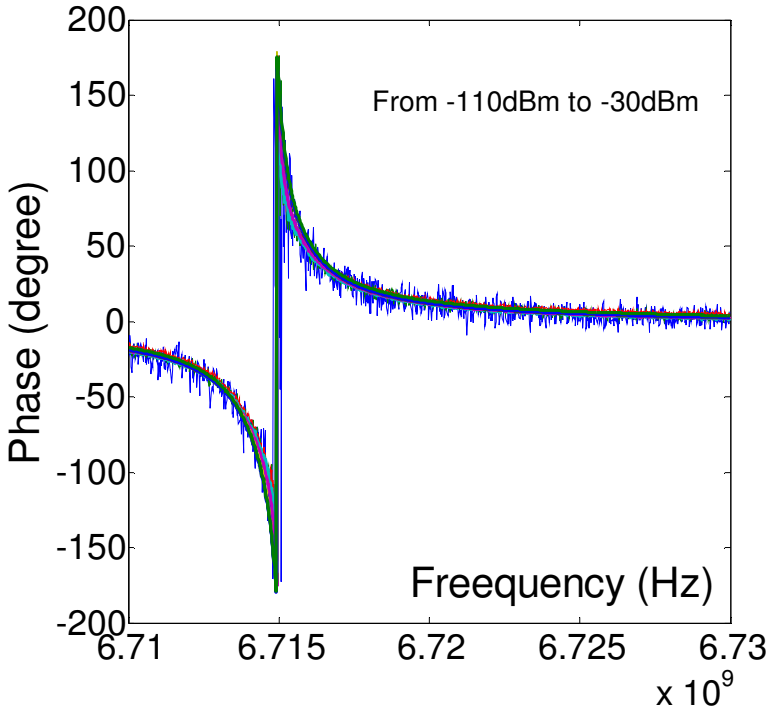

Figure 5.5 Phase response of the Resonator 2 at 300mK for different powers from -110dBm to -30dBm

In the overcoupled case the phase goes from -180^o to +180^o at the resonance frequency, means there is a 360^o of phase change occurs on resonance. While in the undercoupled case the phase change is smaller than 360o when the probe frequency is swept through the resonance. This is shown in figure 5.4 (a) & (b).

We measured the total quality factor for different power values from -110dBm to -30dBm and then using equation (3.19) the internal quality factor Q_{int} can easily be found. The Q_{int} is the measure of loss within the resonator. There are mainly two contributions to this loss; one is resistive losses of the superconductor Q_{r} and the other is dielectric losses Q_d. At low temperatures the surface resistance of the niobium is less than 1μΩ [18] and the corresponding Q_{r} is ~10^6 so at low temperatures Q_{int} is dominated by dielectric losses and can be written as[4]:

$$Q_{\text{int}} \approx Q_d = \frac{1}{\tan\delta}, \qquad (5.5)$$

where tanδ is the loss tangent of the dielectric and is defined as[4]:

$$\tan\delta = \frac{\varepsilon_i}{\varepsilon_r} \qquad (5.6)$$

where ε_r and ε_i are the real and the imaginary parts of the dielectric constant.

Our results of the internal quality factor of **Resonator1** & **Resonator2** show the nonlinear behavior of dielectric losses which decrease with increasing power up to a

certain value as shown in figure 5.6. It means that at lower power values the total quality factor dominated by internal losses which is also shown in figure 5.3 where at low powers resonator is in the undercoupled regime.

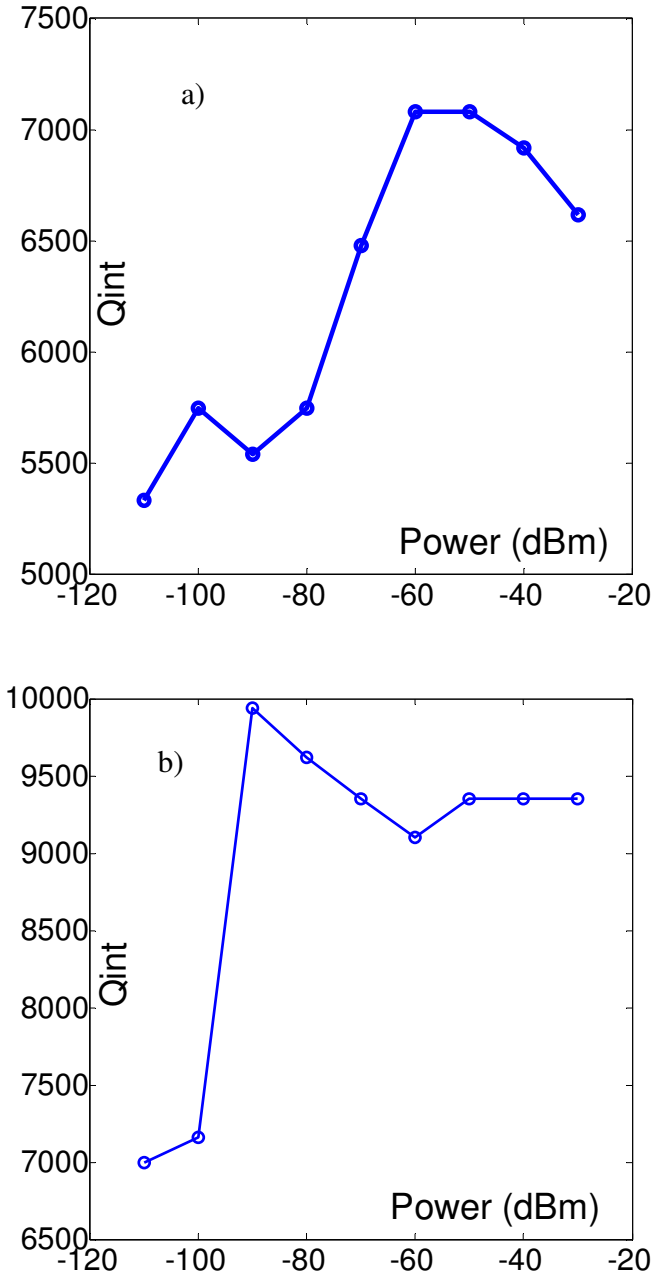

Figure 5.6 Internal quality factor Vs power a) Resonator 1 b) Resonator 2, measured at 300mK

These results are consistent with the reference [22] where they showed the same kind of nonlinear behavior of MgO dielectric losses at low powers at 5K shown in figure 5.7. They observed the same power dependence for both Nb and YBCO on MgO and absence

of this non-linear behavior for sapphire and $LaAlO_3$ which proved their observation are caused by the dielectric response of MgO. They attributed theses effects to a bath of two level states (TLS) defects in MgO which absorb energy at low powers and become saturated at higher powers.

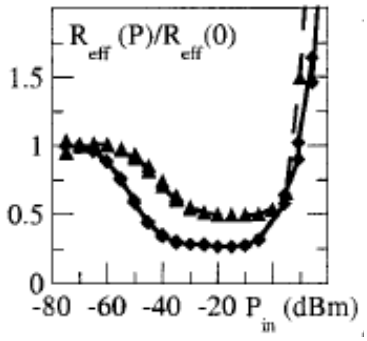

Figure 5.7 Normalized effective resistance vs in put power for the YBCO films (diamonds) and the Nb films on MgO at 5K[22]

Measurements were also taken at various temperatures from 300mK to 8K for -60dBm. The resonance frequency of the resonator remains constant up to a certain value of temperature and after that it starts decreasing. If we measure the phase response of resonator at different temperatures we see that the resonator goes from overcoupled to undercoupled regime as we increased the temperature from 300mK to 8K. This is shown in figure 5.8.

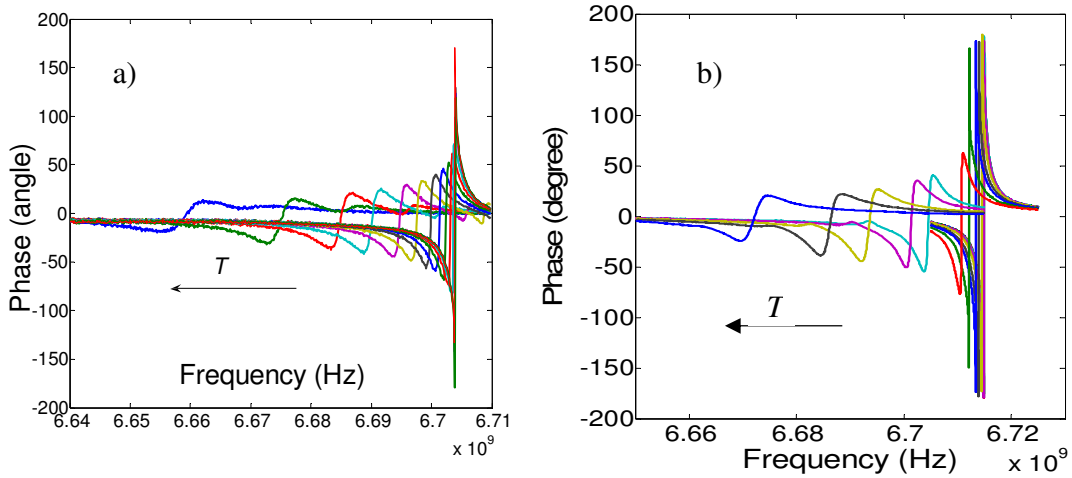

Figure 5.8 phase response of reflection coefficient measured at -60dBm and at different temperatures a) Resonator 1 b) Resonator 2. It shows a transition from overcoupled regime to undercoupled regime as we increase the temperature.

Transition from overcoupled to undercoupled shows that the internal losses increase as we move from lower to higher temperatures. Figure 5.9 shows the internal quality factor as a function of temperature.

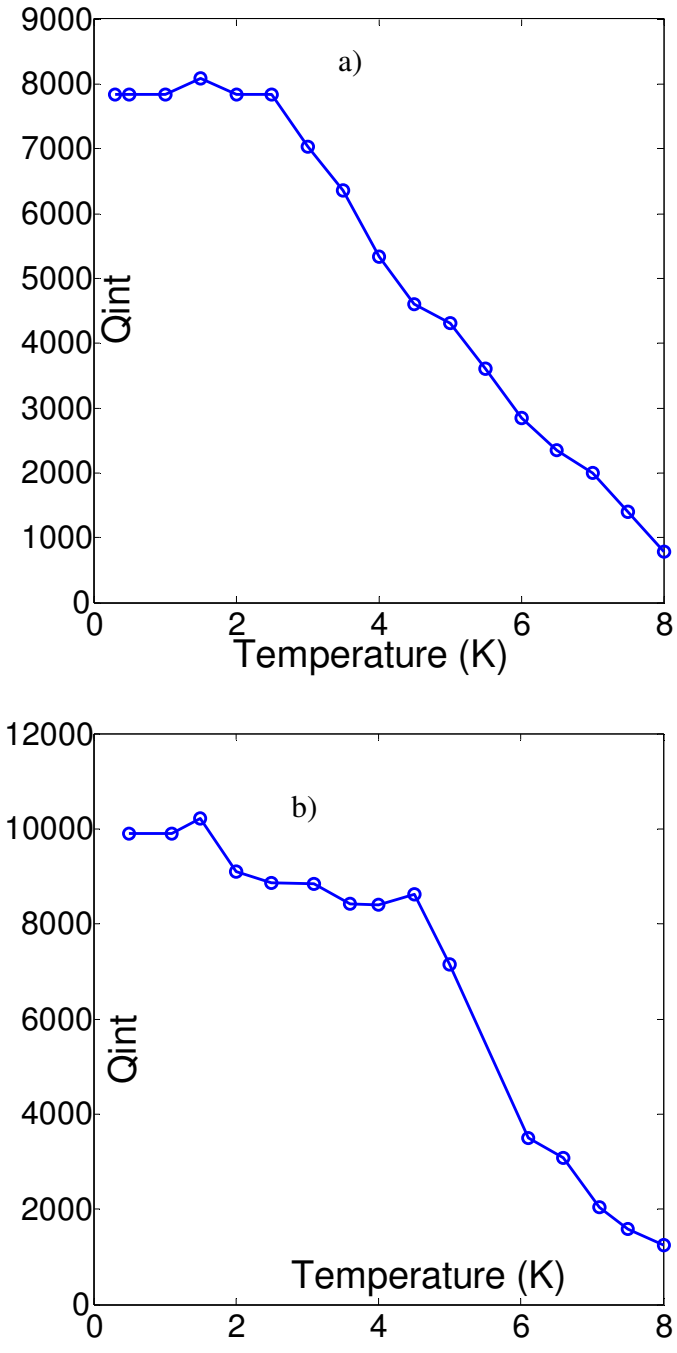

Figure 5.9 Figure 5.6 Q_{int} measured at -60dBm for different temperatures a) Resonator 1 b) Resonator 2.

At -60dBm all the TLS in MgO substrate become saturated as shown in figure 5.6 and once the TLS in dielectric become saturated they do not contribute in the dielectric losses anymore. So in the temperature dependence of the internal quality factor what we see actually is the resistive losses not dielectric losses as we took our temperature dependence at -60dBm. M.A. Hein, in reference [23] showed the temperature dependence of the effective resistance ($R_{eff}=R_s+G\times\tan\delta$, where R_s is the surface resistance of the film and G~0.8 is geometry factor in their case) of YBCO on MgO substrate for two input power values (-60dBm & -20dBm). At lower power they had identified a nonlinear loss mechanism in MgO, which became prominent below about 20K. But at higher power where all the TLS in the dielectric seemed to be saturated they observed an increase in effective resistance with the temperature due to the losses in YBCO films as shown in figure 5.10.

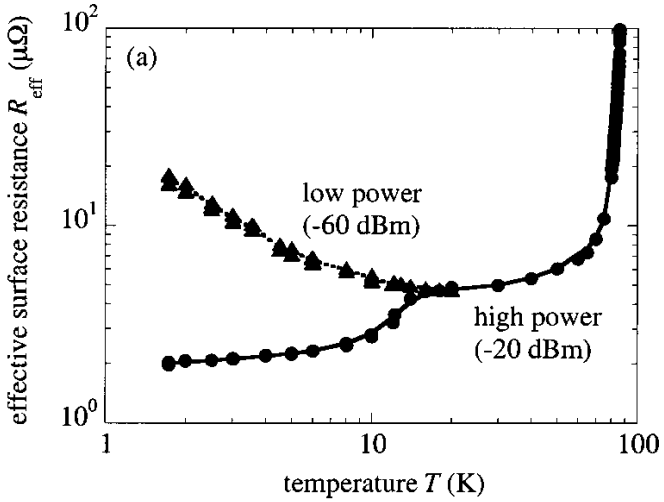

Figure 5.10 Effective surface resistance of YBCO films on MgO as a function of temperature at -20dBm (dots) and -60dBm (triangles)[23]

Information about the London penetration depth λ_L and critical temperature T_c has been obtained from the temperature dependent measurements of the resonance frequency. As we mentioned before the increase in temperature causes the resonance frequency to shift to the lower values due to the increase in kinetic inductance of the resonator as ω_r is a function of kinetic inductance L_{kin}. The resonance frequency is implicitly related to the kinetic inductance of a line as [24]:

$$\frac{f_0(T)}{f_0(T_0)} = \sqrt{\frac{L_{ext} + L_{kin}[\lambda_L(T_0)]}{L_{ext} + L_{kin}[\lambda_L(T)]}} \qquad (5.5)$$

where L_{kin} and L_{ext} are the kinetic and external inductances of the resonator and are given in equations (3.15) & (3.16). And $\lambda_L(T_0)$ is the magnetic penetration depth at the lowest measured temperature, $\lambda_L(T)$ is London penetration depth as a function of temperature

given in equation (3.17) and $f_0(T_0)$ is resonance frequency measured at the lowest temperature. The London penetration depth and critical temperature were evaluated by fitting the normalized resonance frequency given in equation (5.5) to the measured curve (see figure 5.11). The fitting parameters are $\lambda_L(T_0)$ and critical temperature T_c. From fitting we got $\lambda_L(T_0)$ =96nm and T_c=9.2K for **Resonator 1** and $\lambda_L(T_0)$ =94nm and T_c=9.2K for **Resonator 2** which are comparable with the values given in reference [25] where they found the London penetration depth for different thicknesses. For 120nm thick film of niobium they found London penetration depth of 96nm.

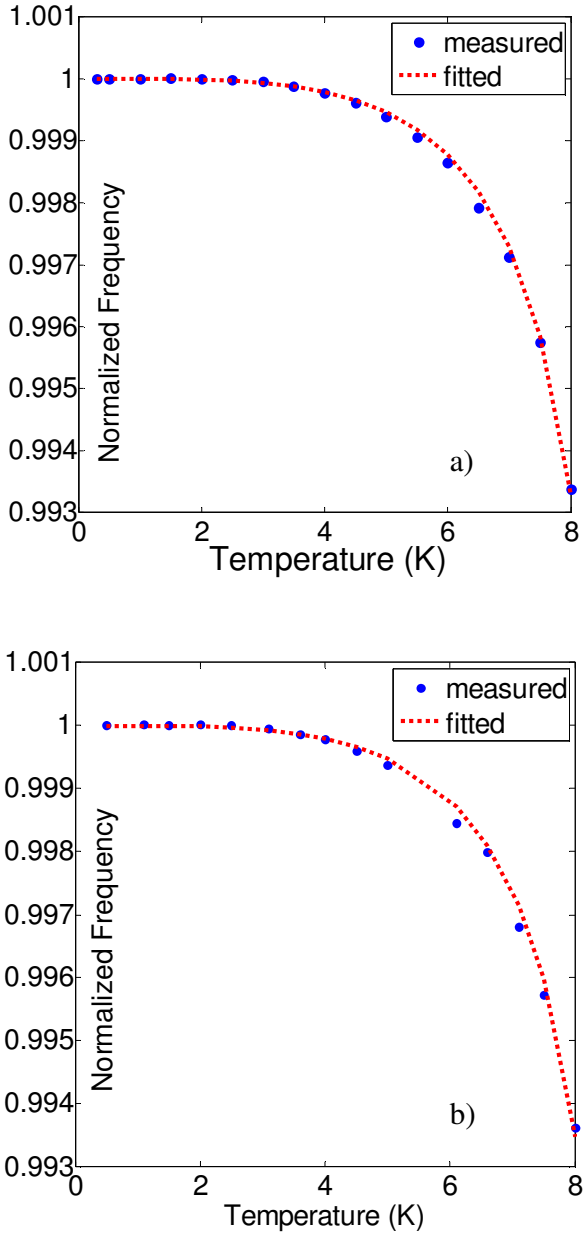

Figure 5.11 Measured and fitted curves of normalized resonance frequency $f_0(T)/f_0(T_0)$ as a function of temperature a) Resonator 1 b) Resonator 2

5.2 Resonator on MgO/STO Combination:

The realization of HTS quantum circuits requires the fabrication of grain boundary Josephson junction, with high quality factors. Here the biepitaxial process is one promising fabrication technique. For the realization of a biepitaxial YBCO grain boundary Josephson junction on a MgO substrate a thin STO seed layer has to be grown on the substrate prior to the deposition of YBCO. In this respect we want to study the dielectric losses of MgO partially coverd with a thin layer of STO. But unfortunately we could not get any useful information because the amplitude curves we got were asymmetric at all powers. And the same for the curves at low temperatures but they look better as we moved to higher temperatures as shown in figure 5.12 & 5.13.

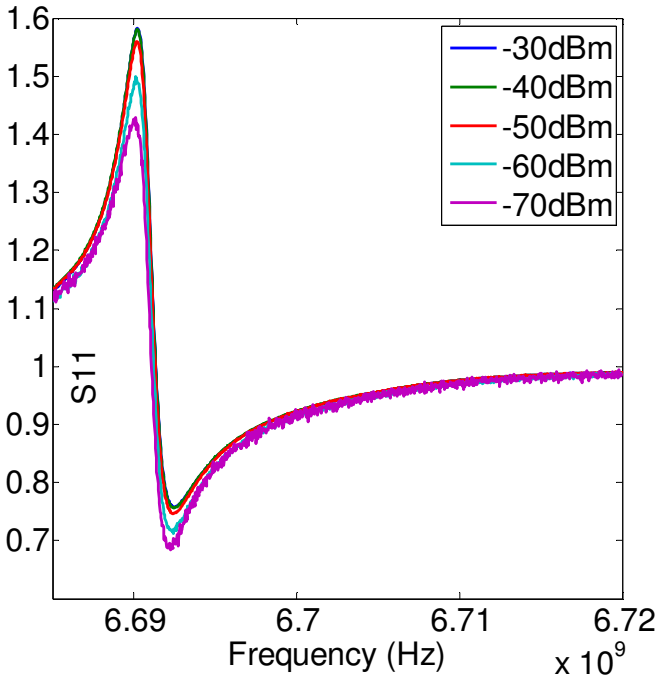

Figure 5.12 S11 asymmetrical curves at different power power. The same behavior holds for other lower values of power not shown in the graph.

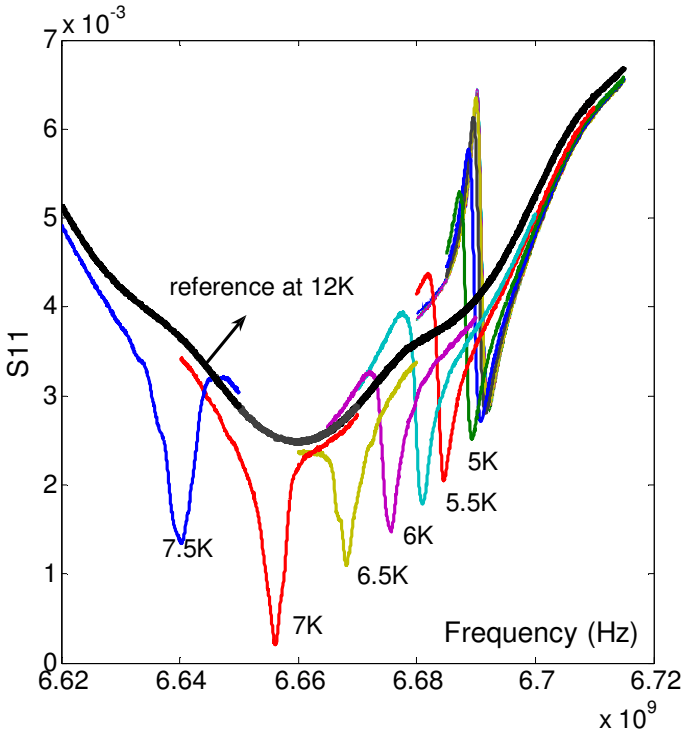

Figure 5.12 S11 measurement curves at different temperatures. They are getting better as we move to higher temperatures.

One reason of these strange curves is may be the problem in our measurement setup but we are not quite sure so far. We are still trying to figure out this problem.

Chapter 6

Conclusion

The main hurdle in the way of LTS and HTS quantum circuitries based on Josephson junctions is the short coherence time in such kind of systems. One source of decoherence is the energy relaxation within the dielectrics on which these junctions are fabricated. The goal of this thesis work is to study the dielectric losses of MgO, suitable for the epitaxial growth of the HTS material YBCO, at very low powers and at millikelvin temperatures which is the operating regime of these kinds of devices. We used superconducting CPW resonator technique to measure the losses of the dielectric mentioned above. The internal quality factor Q_{int} of these kinds of resonators determines the dielectric losses and the losses inside the superconductors. As we took our measurements at very low temperatures (280mK) the losses inside the conductors are very small. So the internal quality factor gives us the information about the dielectric losses in our case. The internal quality factor of MgO has been achieved in the range of 7000-8000 at the very lowest power (-110dBm) and at millikelvin temperatures. It gives the relaxation time in the range of 500-600ns that is enough to use the MgO as dielectric in the HTS quantum devices.

Moreover the information about the London penetration depth and critical temperature of the Niobium has been obtained from the temperature dependence of the resonance frequencies of the resonators. Those values of London penetration depth and critical temperature are consistent with the literature.

Acknowledgements

First of all I would like to thank to my supervisors Dr. Thilo Bauch and Dr. Floriana Lombardi for providing me this opportunity to do my Master's thesis in their group. And especially, to Thilo Bauch, for his many useful suggestions, his guidance and for having complete faith and patience with me during this research. He was always ready to discuss any kind of problem with me and to transmit his broad knowledge in physics and superconductivity.
I would also like to thank to David Gustaffsson who helped me a lot in making masks, SEM scans, AFM scans, film deposition and in other fabrication stuff. I would also like to thank to Shahid Nawaz for helping me in AFM scans. He has been a great support in the whole period of my thesis. I am also thankful to Karin for helping me in photolithography.
I would also like to thank to Martin Sandberg for providing me some fitting curves, helping in microwave measurement setup and for his great discussions and suggestions about the work.
I am also grateful to my parents and my siblings, especially my elder brother Shafqat Mumtaz Virk, for their undying moral and financial support throughout my education and enabling me to become and do all the wonderful things that I have done. Without them this would certainly have not been possible. Last but not the least; I am also grateful to Muhammad Hanif, Alley Hameedi, Hafiz Bilal and Altaf Hussain for being such wonderful friends who have always been there for me, even through the worst of times and have been an incredible source of support and encouragement.
At the end I would also like to thank to whole QDP group at MC2.

References

[1] R.P. Feynman. Simulating Physics with Computers. Int. J. Theor. Phys., V 21:**467**, 1982.

[2] D. Deutsch. Quantum-theory, the Church-Turing principle and the universal quantum computer. Proceedings of the royal society of London series A – mathematical physical and engineering sciences, **400**(1818):97{117, 1985

[3] P. Shor. Algorithms for quantum computation: discrete logarithms and factoring. In Proceedings of the 35th Annual Symposium on Foundations of Computer Science, page **124**, 1994.

[4] John M. Martinis et al. Decoherence in Josephson Qubits from Dielectric losses, PRL 95, **210503** (2005).

[5] M. H. S. Amin et al, "Silent phae qubit based on d-wave Josephson junctions" PR B 71, **064516** (2005)

[6] Thilo Bauch et al "Quantum dynamics of d-wave Josephson junction" Science Vol. 311 pg **57** (2006)

[7] T. Bauch " Macroscopic quantum tunneling in d-wave YBCO Josephson junctions" PRL 4, **087003** (2005)

[8] Aaron D. O'Connell et al, Microwave dielectric loss at single photon energies and millikelvin temperatures, Appl. Phys. Lett. 92, **112903** (2008); doi:10.1063/1.2898887.

[9] F. Lombardi et al. , phys. Rev. Lett. 89, **207001** (2002)

[10] F. Miletto Granozio et al, Structure and properties of a class of CeO_2-based biepitaxial $YBa_2Cu_3O_{7-\delta}$ Josephson junctions, PRB 67, **184506** (2003)

[11] Foundations for Microwave Engineering, 2nd Edition by Robert E. Collin

[12] Microwave and RF Design of Wireless Systems by David M. Pozar

[13] L.M.K. Vandersypen, M. Steffen, G. Breyta, C.S. Yannoni, M.H. Sherwood, and I.L. Chuang, Experimental realization of shor's quantum factoring algorithm using nuclear magnetic resonance, Nature **414** (2001), 883–887.

[14] R. N. Simons, Coplanar Waveguide Circuits, Components, and Systems, John Wiley & Sons, (New York), 2001.

[15] Julia M. Phillips ,"Substrate selection for high-temperature Superconducting thin films" Appl. Phys. **79**(4), 15 Feb. 1996

[16] Superconducting coplanar delay lines by Yi Wang PhD thesis The University of Birmingham.

[17] W.Raucg and E. Gornik, "Microwave properties of YBCO thin films studied with coplanar transmission line resonators", Appl. Phys. **73**(4) Feb. 1993

[18] Theodore Van Duzer & Charles W. Turner, Superconducting devices and circuits, 2nd edition.
[19] A.Wallraff, D.I. Schuster, A. Blais, L. Frunzio, R.-S. Huang, J. Majer, S. Kumar, S.M. Girvin, and R.J. Schoelkopf, Strong coupling of a single photon to a superconducting qubit using circuit quantum electrodynamics, Nature **431** (2004), 162–167.
[20] Martin Sandberg, Tunable Superconducting Resonators for qubit coupling, PhD licentiate thesis, Department of Microtechnology and Nanoscience quantum device physics laboratory Chalmers University of Technology Sweden
[21]http://www.oxford-instruments.com/products/low-temperature/3he refrigerators/helioxvl/Pages/helioxvl.aspx
[22] M.A. Hein, D.E. Oates, P.J. Hirst and R.G. Humphreys ," Nonlinear microwave losses in MgO Substrates". Apl. Physics Letters, Vol. 80 pg **1007 2001**.
[23] M.A. Hein, R.G. Humphreys, P.J. Park, and D.E. Oates, "Nonlinear microwave response of Epitaxial YBCO films of Varying Oxygen Content on MgO Substrates". Journal of Superconductivity: Incorporating Novel Magnetism, Vol. 16, No. 5, October 2003.
[24] W. Rauch and E. Gornik, "Microwave properties of YBCO thin films studied with coplanar transmission line resonators".
[25] A. I. Gubin et al " Dependence of magnetic penetration depth on the thickness of superconducting Nb filims " PR B **72 ,064503** (2005)

Appendix

Matlab Prgram Z_c vs gap width

```
%resonance frequency
f=6.4e9;
%relative dielectric constant
er=11.1;
%width of conductor in micron
w=37.6;
%gap widths
g=0:300;
%height of substrate
h=500;
for i=1:301
s(i)=2*g(i)+w;
k1(i)=w/s(i);
k2(i)=sinh((pi/4)*(w/h))/sinh((pi/4)*(s(i)/h));
k11(i)=sqrt(1-k1(i)^2);
k22(i)=sqrt(1-k2(i)^2);
K1(i)=ellipke(k1(i));
K11(i)=ellipke(k11(i));
K2(i)=ellipke(k2(i));
K22(i)=ellipke(k22(i));
K(i)=K11(i)*K2(i)/K1(i)/K22(i);
ef(i)=(1+(er*K(i)))/(1+K(i));
Z(i)=(60*pi/sqrt(ef(i)))/((K1(i)/K11(i))+(K2(i)/K22(i)));
%i=i+1;
end
%effective dielectric constnt

plot(g,Z)
xlabel('gap width, g (micron)')
ylabel('impedance, Zc (ohm)')
```